Postprint of: Jasiński M., Mul M., Lamęcki A., Gomez-Garcia R., Mrozowski M., Dispersive Delay Structures With Asymmetric Arbitrary Group-Delay Response Using Coupled-Resonator Networks With Frequency-Variant Couplings, IEEE TRANSACTIONS ON MICROWAVE THEORY AND TECHNIQUES Vol. 70, iss. 5 (2022), pp. 2599-2609, DOI: 10.1109/TMTT.2022.3152503

Dispersive Delay Structures With Asymmetric Arbitrary Group-Delay Response Using Coupled-Resonator Networks With Frequency-Variant Couplings

Maciej Jasinski, *Graduate Student Member, IEEE*, Martyna Mul, Adam Lamecki, *Senior Member, IEEE*, Roberto Gómez-García, *Senior Member, IEEE*, and Michal Mrozowski, *Fellow, IEEE*

***Abstract*—This paper reports the design of coupled-resonator-based microwave dispersive delay structures (DDSs) with arbitrary asymmetric-type group-delay response. The design process exploits a coupling-matrix representation of the DDS circuit as a network of resonators with frequency-variant couplings (FVCs). The group-delay response is shaped by using the complex transmission zeros (TZs) created by the dispersive cross-couplings. We also present an optimization-based synthesis procedure for the characteristic polynomials with a prescribed group-delay profile. Thus, when compared to prior-art DDS approaches, the proposed DDS solutions allow a general group-delay profile to be patterned while incorporating optimization-based coupling-matrix-design techniques for their synthesis. The design method is validated by full-wave simulations and measurements of three built proof-of-concept prototypes of DDS devices with different shapes of group-delay response in waveguide and microstrip technologies.**

***Index Terms*—Analog signal processing (ASP), complex transmission zero (TZ), coupling matrix, dispersive delay structure (DDS), frequency-variant coupling (FVC), group delay, microstrip filter, passive circuit, planar filter, waveguide filter.**

I. Introduction

OVER THE last few decades, a rapid growth has taken place in the telecommunications sector visible through the vast number of deployed services and their users. However, spectral resources are limited and in very-high demand due to the ever-increasing amounts of transmitted data. As such, an urgent solution for properly handling such large volumes of information is needed. RF wireless systems are thus evolving towards higher frequency bands. Nevertheless, despite the idea of exploiting as-yet unused spectral resources may seem very simple, it has significant implications and involved challenges at the technological and RF-system-implementation levels.

One of the most severe consequences of this migration to higher spectral bands directly affects the digital blocks of systems that are responsible for signal-processing tasks. Any digital-signal-processing (DSP) unit needs analog-to-digital (ADC) and digital-to-analog (DACs) converters, and it is well known that as their operational frequency increases, DC-power consumption grows, and also heat-dissipation issues become prominent. Thus, to cope with these problems that are intrinsic to processing the signal in the digital domain, the area of analog signal processing (ASP), that seemed to be bound to become obsolete in digital communication systems, has recently been attracting considerable renewed attention.

ASP systems have several advantages over those relying on the DSP philosophy. First, as ASP is based on the analog form of the signal, no signal conversion to the digital domain is needed. Moreover, ASP systems operate in real time. In fact, the differences between ASP and DSP systems become more evident when they are compared while performing the same processing function over the signal. Even if the resulting output signal is the same in both cases, much-higher complexity appears in the DSP approach as the input signal has to be converted to digital, processed, and reconverted back to the initial analog form. On the contrary, all operations in the ASP system are performed directly over the input analog signal without any conversion. Furthermore, ASP can be implemented in passive devices, greatly reducing the overall DC-power consumption of the system. Besides, as an added benefit, it should be remarked upon that some ASP technological implementations can support higher-power applications—for example, those in waveguide technology—when compared to their DSP counterparts. All these merits make the ASP framework very attractive for the implementation of a rich variety of signal-processing functionalities, and various studies about the applications of ASP systems have been already presented. Among them, frequency discriminators [1]–[3], tunable delay lines [4], signal-to-noise-ratio-enhancement blocks [5], extension, compression, and reversal of signals [6], [7], frequency-division-multiplexing (FDM) receivers [8], antenna-array feeding networks [9], and real-time multiple access methods for high-speed communications [10]. A comprehensive overview of ASP devices for microwave applications and the discussion of available technologies can be found in [11].

The key element of most of previously-referred ASP systems is the dispersive delay structure (DDS). It consists of a device that introduces frequency-dependent delays to the

Manuscript received August 23, 2021; revised November 30, 2021; accepted January 30, 2022. Manuscript received in final form on February 4, 2022. This work was supported by the National Science Centre, Poland (UMO-2019/33/B/ST7/00889).

M. Jasinski, M. Mul, A. Lamecki, and M. Mrozowski are with the Faculty of Electronics, Telecommunications, and Informatics, Gdańsk University of Technology, 80-233 Gdańsk, Poland (e-mail: maciej.jasinski@pg.edu.pl; martyna.mul@pg.edu.pl; adam.lamecki@ieee.org; m.mrozowski@ieee.org).

R. Gómez-García is with the Department of Signal Theory and Communications, Polytechnic School, University of Alcalá, 28871 Alcalá de Henares, Spain (e-mail: roberto.gomez.garcia@ieee.org).

$$\boldsymbol{M} = \begin{bmatrix} 0 & 1.6234 & 0 & 0 & 0 & 0 & 0 & 0 \\ 1.6234 & \Omega + 0.5707 & 1.7261 & -0.3435\Omega - 0.8917 & 0 & 0 & 0 & 0 \\ 0 & 1.7261 & \Omega + 1.3206 & 1.3586 & 0 & 0 & 0 & 0 \\ 0 & -0.3435\Omega - 0.8917 & 1.3586 & \Omega + 0.3564 & 1.8785 & 0 & 0 & 0 \\ 0 & 0 & 0 & 1.8785 & \Omega - 0.2660 & 1.3934 & -0.4273\Omega + 1.0719 & 0 \\ 0 & 0 & 0 & 0 & 1.3934 & \Omega - 1.4117 & 2.0635 & 0 \\ 0 & 0 & 0 & 0 & -0.4273\Omega + 1.0719 & 2.0635 & \Omega - 0.8670 & 1.8966 \\ 0 & 0 & 0 & 0 & 0 & 0 & 1.8966 & 0 \end{bmatrix} \tag{1}$$

different spectral components of the signal. The group-delay characteristic of the DDS depends on the specific application of the overall system in which it is integrated. For example, it should exhibit a stepped-type/staircase-like profile in the case of spectrum sniffers [12] and a linear-type shape for the case of real-time-fourier-transform (RTFT) blocks based on the temporal envelope [13]. In other scenarios, even more-complex group-delay frequency patterns could be required. In DDSs, in order to provide unequivocal discrimination of the spectral components of the signal to be processed, a unique delay value must be assigned to each specific frequency or to each frequency sub-band. This means that the DDS group-delay characteristic has to be a monotonic or an absolutely-monotonic function of frequency within the bandwidth of interest.

In the technical literature, several strategies to implement DDS devices have been reported. For example, circuits exhibiting a frequency-variant group-delay response can be realized in microstrip or waveguide technologies as reflection-type DDSs [14]–[17]. However, an additional circulator or coupler is needed in such approach to separate the incident and reflected signals, which increases the overall circuit complexity and size. Alternatively, transmission-type DDSs can be designed by employing C-sections [18]–[20] or coupled-line stages [21] with all-pass behavior over wide frequency ranges. Nevertheless, their planar implementation limits their use to low-frequency and low-power applications. Moreover, the group-delay resolution is poor in such DDS devices when their operational bandwidth is relatively narrow. A third choice, which also belongs to the category of transmission-type DDSs, consists of exploiting coupled-resonator networks as in bandpass filters [22], [23]. As associated benefits, coupled-resonator-based DDSs can be implemented at higher frequency ranges by using waveguide technology so that to process higher-power signals, while also offering superior narrowband group-delay resolution and lower loss when compared to their C-section counterparts. In this variant, the selectivity and the equiripple-type return-loss profiles are not enforced in the design process, as it is mainly the phase characteristic that is of interest. The frequency-dependent group-delay pattern can be shaped in these DDSs by engineering their networks so as to exhibit transfer functions with complex transmission zeros (TZs). The positions of these complex TZs in their coupled-resonator circuits are controlled with the selection of a suitable coupling-routing scheme and by the sign and magnitude of their inter-resonator couplings. A summary of the main advantages and disadvantages of the different classes of DDSs is provided in Table I.

In this paper, we propose a new approach to the design and implementation of DDSs. Specifically, the DDSs are realized

TABLE I
COMPARISON OF VARIOUS DDS DESIGN APPROACHES

Approach	Pros	Cons
C-section transmission type [18]–[20]	Asymmetric response and broadband operation	Low-frequency/low-power applications and poor narrowband resolution
Reflection type	Broadband operation [14], [16], compact design [15], and applicable to high frequencies [17]	Need for extra signal-separation device
Coupled-chirped-line transmission type [21]	broadband operation	high insertion losses
Coupled-resonator transmission type [22], [23]	Design based on coupling matrix, good narrowband resolution, applicable to high frequencies, and flexible topology	Narrowband behavior

in this study as coupled-resonator circuits as in [22], [23], while using optimization-based coupling-matrix synthesis for their design. We focus on asymmetric-type group-delay responses and, unlike in related previously-published works [22], [23], we allow the inter-resonator couplings to vary with frequency. Note that frequency-dependent couplings have recently attracted considerable attention by the microwave filter community as a new way to generate TZs—both imaginary and complex [24]–[36]. One advantage of this TZ-creation mechanism in microwave filter design is that it allows simpler circuit typologies and gives more flexibility in terms of the number of created TZs and their positions. For instance, in an inline coupling scheme, a frequency-variant coupling (FVC) introduces one TZ on the $j\omega$ axis, which cannot be produced by such topology when only employing frequency-invariant couplings (FICs)—the creation of a single TZ requires at least a triplet when just using FICs. Moreover, if a triplet topology is considered that is capable of providing one imaginary TZ for FICs, introducing one FVC brings about a pair of complex TZs. This is particularly useful for group-delay equalization purposes [30], [31]. In order to provide a better idea of the benefits that can be obtained by means of dispersive couplings, Table II compares a few different-order filter configurations [33] with and without FVCs. In this table, resonators are designated by black circles, constant couplings—i.e., FICs—are denoted by straight lines, and FVCs are represented by crossed lines with an arrow. It can be observed that, by introducing a dispersive coupling, the filter topologies are simplified while the number of TZs of their filter characteristics is increased as major advantages. For example, a triplet with one constant

$$\boldsymbol{M} = \begin{bmatrix} 0 & 0.9773 & 0 & 0 & 0 & 0 & 0 \\ 0.9773 & \Omega - 0.0869 & 0.9195 & 0 & 0 & -0.1650\Omega - 0.0399 & 0 \\ 0 & 0.9195 & \Omega - 0.0451 & 0.5324 & -0.2854\Omega - 0.0982 & 0 & 0 \\ 0 & 0 & 0.5324 & \Omega + 0.1066 & 0.5527 & 0 & 0 \\ 0 & 0 & -0.2854\Omega - 0.0982 & 0.5527 & \Omega - 0.0384 & 1.3686 & 0 \\ 0 & -0.1650\Omega - 0.0399 & 0 & 0 & 1.3686 & \Omega - 0.1468 & 1.4889 \\ 0 & 0 & 0 & 0 & 0 & 1.4889 & 0 \end{bmatrix} \tag{2}$$

cross-coupling that produces a single TZ on the $j\omega$ axis can be replaced by an inline doublet with one FVC. Introducing just one FVC in a triplet brings about two TZs on the imaginary ω axis or one pair of complex TZs that are placed symmetrically with regard to the imaginary axis. However, a filter network without FVCs requires a total of four resonators and two cross-couplings to produce the same effect.

TABLE II
FILTER TOPOLOGY OVERVIEW

Topology	TZs
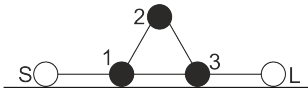	1 TZ (imaginary axis)
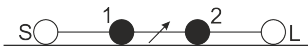	1 TZ (imaginary axis)
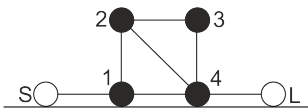	2 TZs (imaginary axis) or 1 pair of complex TZs
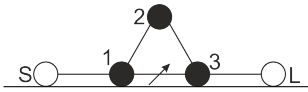	2 TZs (imaginary axis) or 1 pair of complex TZs

To the best of our knowledge, DDSs implemented as coupled-resonator networks using FVCs have not been considered to date. In this work, we present a design process for such DDS structures with arbitrary group-delay characteristics, including asymmetric-type profiles. As expounded in Sections II and III, respectively, their design procedure involves two main steps: (i) the synthesis of a rational function that exhibits the required group-delay characteristic, followed by (ii) the synthesis of the coupling matrix with FVCs. Both steps involve optimization and result in the final coupled-resonator network with FVCs featuring the intended group-delay profile. In Section IV, in order to validate the design method and demonstrate the advantages of using FVCs, we design and fabricate three proof-of-concept prototypes of DDSs in waveguide and microstrip technologies based on coupled-resonator networks with different type of asymmetric group-delay profile.

II. SYNTHESIS OF THE CHARACTERISTIC POLYNOMIALS FOR ASYMMETRIC GROUP-DELAY PROFILE

The first step in the synthesis procedure is to construct a rational function that provides the desired group-delay profile for the transfer function of the device. A DDS implemented as a network of coupled resonators may be regarded as a special type of bandpass filter for which the phase characteristic must be engineered, while the amplitude restrictions are not strictly enforced. For instance, equiripple and selectivity conditions are not imposed. The behaviour of the filter can be described in a very convenient way by two rational functions as follows:

$$S_{11} = \frac{F(s)}{E(s)} \qquad S_{21} = \frac{P(s)}{E(s)} \tag{3}$$

where $s = \sigma + j\Omega$ is the complex normalized frequency. The roots of $F(s)$ and $P(s)$ determine the locations of the reflection and TZs. In particular, it should be emphasized that the roots of $P(s)$ are located symmetrically with regard to the imaginary axis of the complex plane. Therefore, the phase characteristic of the numerator of S_{21} is constant with frequency and, in consequence, the group-delay variation pattern is determined exclusively by the common denominator $E(s)$ [23]. The polynomial $E(s)$ thus defines the overall phase characteristic, and needs to be synthesized in order to fit the required group-delay frequency-variation profile. For symmetric-type phase responses, the design procedure is deterministic, as demonstrated in [23]. However, in this work, we concentrate on DDSs with asymmetric-type group-delay frequency-variation pattern that are needed in some ASP applications to provide an unambiguous distinction of the spectral components of the signal.

As mentioned above, a deterministic procedure to design coupled-resonator-based DDSs with asymmetric-type group-delay profile is not known, so the polynomial $E(s)$ has to be found through optimization. The starting point of the optimization process is a polynomial $E(s)$ associated to a Chebyshev filter with the same parameters as the target DDS, but with no requirements imposed on the group-delay response. The target group-delay characteristic τ_{spec} is sampled at M normalized frequency points $[\tau_{spec}(\Omega_0), \tau_{spec}(\Omega_1), ..., \tau_{spec}(\Omega_M)]$ where $\Omega_i \in [-1, 1]$. The roots of the polynomial $E(s)$ are then varied in the complex plane until the phase profile fits the intended group-delay response. This is done by finding the minimum of a goal function defined as the difference between the target values of the group delay and the values of the group delay in the ongoing iteration. This goal function has the following form:

$$c = \sum_{i=0}^{M} \Big(\tau(\Omega_i) - \tau_{spec}(\Omega_i)\Big)^2. \tag{4}$$

Note that with the above cost function, the in-band return-loss level is not controlled during the optimization process. If the minimum in-band return-loss-level value of the achieved response is not satisfactory, an additional term RL_{cost} can be

$$\boldsymbol{M} = \begin{bmatrix} 0 & 0.9649 & 0 & 0 & 0 & 0 & 0 \\ 0.9649 & \Omega + 0.0674 & 0.9022 & 0 & 0 & 0.1872\Omega - 0.0612 & 0 \\ 0 & 0.9022 & \Omega - 0.0575 & 0.5143 & 0.2870\Omega - 0.1117 & 0 & 0 \\ 0 & 0 & 0.5143 & \Omega - 0.2419 & -0.5455 & 0 & 0 \\ 0 & 0 & 0.2870\Omega - 0.1117 & -0.5455 & \Omega - 0.1138 & 1.4141 & 0 \\ 0 & 0.1872\Omega - 0.0612 & 0 & 0 & 1.4141 & \Omega - 0.0292 & -1.5430 \\ 0 & 0 & 0 & 0 & 0 & -1.5430 & 0 \end{bmatrix} \quad (6)$$

added to this goal function for its optimization as follows:

$$RL_{cost} = \begin{cases} (|S_{11}|^{max} - |S_{11}|^{goal})^2, & \text{if } |S_{11}|^{max} > |S_{11}|^{goal} \\ 0, & \text{otherwise} \end{cases} \quad (5)$$

where $|S_{11}|^{goal}$ is the goal related to the maximum allowed value for $|S_{11}|$ in the passband and $|S_{11}|^{max}$ is the maximum in-band value of $|S_{11}|$ at the current optimization iteration. It should be remarked upon that the goal function just imposes the minimum in-band return-loss level to be fulfilled, so that responses with improved return-loss-level values with regard to this minimum can be found through the optimization process. Once the minimum has been reached and the polynomial $E(s)$ has been derived, the polynomials $F(s)$ and $P(s)$ can be calculated using the deterministic procedure described in [23]. It is worthwhile to observe that since the polynomial $F(s)$ is constructed from the polynomials $E(s)$ and $P(s)$, we cannot guarantee that its roots will be located on the imaginary axis as it happens in filters with generalized-Chebyshev-type response.

In order to illustrate the synthesis of polynomials under the condition of a required minimum in-band return-loss level, we present a design example of a DDS with linear-type group-delay profile. The parameters of the target polynomials are: order $N = 5$, minimum in-band return-loss level $RL = 20$ dB, slope of the linear-group-delay response of 0.4 s/Hz, and two pairs of complex TZs distributed symmetrically with regard to the imaginary axis. For the optimization, we used a gradient-based procedure. The algorithm finds the solution reaching the required value of the error function (10^{-6}) within 61 iterations. The power transmission, reflection, and group-delay responses of the designed filter-based DDS, calculated using the initial and final polynomials, are plotted in Fig. 1. Note that the in-band return-loss levels—while not equiripple-type—do not exceed the prefixed 20-dB value.

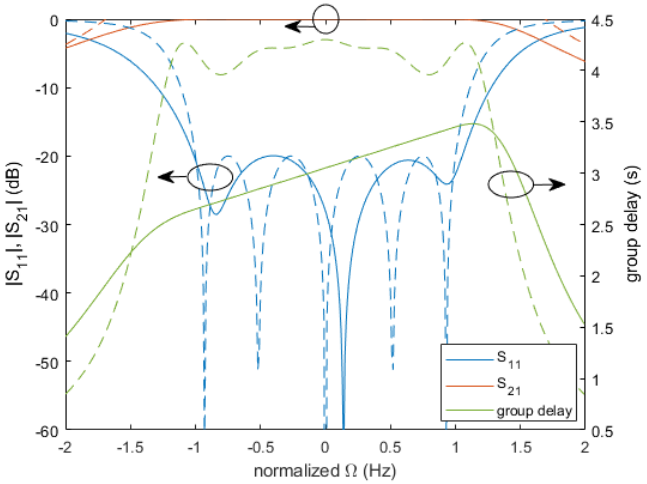

Fig. 1. Power-transmission ($|S_{21}|$), reflection ($|S_{11}|$), and group-delay responses of the filter-based DDS calculated from polynomials (dashed lines: initial polynomials; solid lines: final polynomials).

III. Synthesis of the Coupling Matrix

Once the polynomials are known, the coupling matrix for the coupled-resonator network with FVCs can be synthesized using the procedure described in [37]. Assuming that couplings are allowed to vary linearly with frequency, the relationship between the scattering parameters and matrix $\boldsymbol{M} = \boldsymbol{M_0} + \Omega \boldsymbol{M_1}$ that provides information related to couplings and resonator detuning can be described through the following equations:

$$S_{11} = 1 + 2jR_S \frac{\det(\boldsymbol{M_0}' - j\boldsymbol{R}' + \Omega \boldsymbol{M_1}')}{\det(\boldsymbol{M_0} - j\boldsymbol{R} + \Omega \boldsymbol{M_1})} \quad (7)$$

$$S_{21} = -2j\sqrt{R_S R_L} \frac{\det(\boldsymbol{M_0}'' - j\boldsymbol{R}'' + \Omega \boldsymbol{M_1}'')}{\det(\boldsymbol{M_0} - j\boldsymbol{R} + \Omega \boldsymbol{M_1})} \quad (8)$$

where $R_S = R_L = 1$ are the normalized source and load impedances, $\boldsymbol{R}$ is equal to zero except for the first and last diagonal elements—which are equal to R_S and R_L, respectively—, $\boldsymbol{M_0}$ is the frequency-invariant coupling matrix of size $N + 2$ by $N + 2$—N is the number of resonators—, and $\boldsymbol{M_1}$ is the $N + 2$ by $N + 2$ matrix with elements on its diagonal equal to 1—except the first and last one which are zero—and whose off-diagonal entries describe the couplings that are linearly dependent with frequency. Matrices with the prime symbol are created by deleting the last row and column from their associated $\boldsymbol{M_0}$, $\boldsymbol{M_1}$, and $\boldsymbol{R}$ matrices. Matrices with the double prime symbol are constructed in the same way, but the first row and last column are deleted instead.

Equations (7) and (8) when compared to (3) reveal the relationship existing between the roots of the characteristic polynomials and the eigenvalues of the corresponding matrix pencils: the zeros of $P(s)$ are equal to the eigenvalues of the pencil $([\boldsymbol{M_0}'' - j\boldsymbol{R}''], \boldsymbol{M_1}'')$, while the zeros of $E(s)$ are the eigenvalues of $([\boldsymbol{M_0} - j\boldsymbol{R}], \boldsymbol{M_1})$. It is easy to demonstrate that the roots of the polynomial $G(s) = F(s) - E(s)$ are the eigenvalues of $([\boldsymbol{M_0}' - j\boldsymbol{R}'], \boldsymbol{M_1}')$.

Using the above mathematical expressions, we can formulate a goal function for the coupling-matrix optimization as follows:

$$C = ||\boldsymbol{\lambda_0} - \boldsymbol{\lambda}||_2 \quad (9)$$

where $\boldsymbol{\lambda_0}$ is a vector of roots of the characteristic polynomials of the target network response, $\boldsymbol{\lambda}$ is a vector of eigenvalues

$$\boldsymbol{M} = \begin{bmatrix} 0 & -1.2212 & 0 & 0 & 0 \\ -1.2212 & 1.4645\Omega - 0.0229 & -1.1221 & 0.4645\Omega - 0.2907 & 0 \\ 0 & -1.1221 & \Omega - 0.3127 & 1.3768 & 0 \\ 0 & 0.4645\Omega - 0.2907 & 1.3768 & 1.4645\Omega - 0.2612 & 1.7614 \\ 0 & 0 & 0 & 1.7614 & 0 \end{bmatrix} \tag{10}$$

of the referred matrix pencils at a certain iteration step, and $||\cdot||_2$ denotes the L2-norm. The optimized variables are the elements of the $\boldsymbol{M_0}$ and $\boldsymbol{M_1}$ coupling matrices. The positions of the nonzero entries of the coupling matrices are defined by the target filter topology.

As an illustrative example of this approach and in order to show the benefits of using FVCs, we consider two different implementations of an intended DDS design. Fig. 2 depicts two alternative coupled-resonator topologies for this DDS design, both of them with the same response. The first network in 2(a) corresponds to the DDS presented in [23] that consists of a sixth-order structure in a folded-form topology. Using a folded coupled-resonator structure brings some geometrical restrictions in the physical implementation, thus limiting the choice of the technology. The same group-delay characteristic can be obtained in a much simpler circuit that comprises two cascaded triplets as shown in Fig. 2(b), each of them having one frequency-dependent cross-coupling. For completeness, we give in (1) the resulting matrix $\boldsymbol{M} = \boldsymbol{M_0} + \Omega \boldsymbol{M_1}$ for the designed DDS network with FVCs in Fig. 2(b). The coupling matrix for the circuit in Fig. 2(a) based on the folded arrangement of resonators can be found in [23].

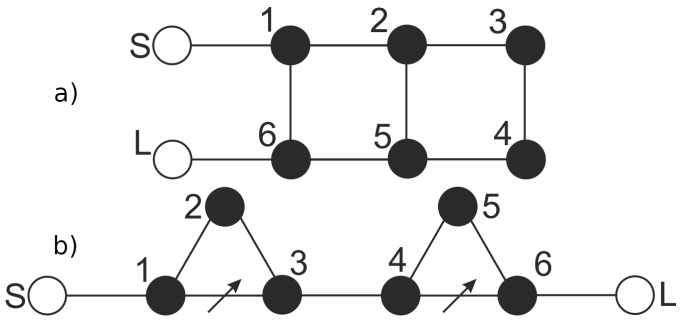

Fig. 2. Two alternative topologies for a sixth-order filter-based DDS with the same response (black circles: resonators; white circles: source and load; lines: couplings; lines with arrows: FVCs).

Another example is a fifth-order coupled-resonator-based DDS with two frequency-variant cross-couplings, that features a linear-type group-delay response with a negative slope coefficient and minimum in-band return-loss level $RL = 16$ dB. The coupling matrix for this DDS design, which was found by using the method previously described, is provided in (2). The power transmission, reflection, and group-delay responses of the designed DDS, calculated from both the obtained coupling matrix and polynomials, are compared in Fig. 3. Its associated coupling-routing diagram is also depicted in Fig. 3 as an inset.

IV. Design of DDSs with Asymmetric-Type Group-Delay Responses and Measurements

In order to demonstrate the potential and accuracy of the proposed synthesis method for coupled-resonator-based DDSs with FVCs, as well as the practical viability of the resulting DDS configurations, three different DDS devices with arbitrary asymmetric-type group-delay profiles were designed, fabricated, and characterized. One prototype was implemented in waveguide technology, whereas the other two were developed using microstrip technology. These three DDS circuits should be regarded as proof-of-concept prototypes as they were implemented by means of in-house manufacturing processes.

A. Fifth-Order Waveguide DDS

The first device is a fifth-order coupled-resonator DDS with center frequency $f_0 = 10$ GHz, bandwidth $BW = 200$ MHz, and minimum in-band return-loss level $RL = 16$ dB. It has a linear-type group-delay characteristic with swing over the referred bandwidth equal to $\Delta\tau = 1.496$ ns, a slope coefficient of 7.48 ns/GHz, and a resolution equal to $\varrho = \Delta\tau \cdot BW = 0.293$. This DDS response can be used in frequency-discrimination systems. Note that this design example is analogous to the fifth-order DDS example with negative group-delay slope considered in Section II, but in this case the slope coefficient sign is selected to be positive. Thus, we assume the same coupled-resonator topology with FVCs for its design as before—inset of Fig. 3. It includes two dispersive cross-couplings inserted between the first and fifth resonators and between the second and fourth resonators. The dispersive couplings generate two pairs of complex TZs to shape the intended group-delay response.

The roots of the characteristic polynomials of this filter-based DDS were found by applying the optimization process described in Section II and they are listed in Table III. Note that the resulting reflection zeros—i.e., roots of the polynomial $F(s)$—are complex. The coupling matrix was derived using the method from [37] and has the form of (6). Fig. 4 compares the power transmission, reflection, and group-delay characteristics in the normalized frequency domain Ω, calculated from both the polynomials and the coupling matrix. As can be seen, the responses from both models are practically identical.

The circuit was implemented using the WR90 waveguide standard. The initial dimensions of the physical structure were found with a classical coupling extraction technique [38] by simulating each coupling separately. For the dimensional synthesis of the dispersive couplings, we used the approach described in [27]. Although the initial result was far from the desired response, it sufficed as a starting point for the optimization process. The full-wave optimization was carried out in InventSIM—3D FEM commercial software—using a

$$\boldsymbol{M} = \begin{bmatrix} 0 & 1.0723 & 0 & 0 & 0 & 0 & 0 \\ 1.0723 & 1.7201\Omega - 0.0863 & 0.7835 & 0.7201\Omega - 0.5876 & 0 & 0 & 0 \\ 0 & 0.7835 & \Omega - 0.4154 & -0.8604 & 0 & 0 & 0 \\ 0 & 0.7201\Omega - 0.5876 & -0.8604 & 2.6460\omega + 0.4162 & -1.0701 & 0.9259\omega + 0.8685 & 0 \\ 0 & 0 & 0 & -1.0701 & \Omega + 0.6109 & 1.4618 & 0 \\ 0 & 0 & 0 & 0.9259\Omega + 0.8685 & 1.4618 & 1.9259\Omega + 1.2792 & 1.8432 \\ 0 & 0 & 0 & 0 & 0 & 1.8432 & 0 \end{bmatrix} \quad (11)$$

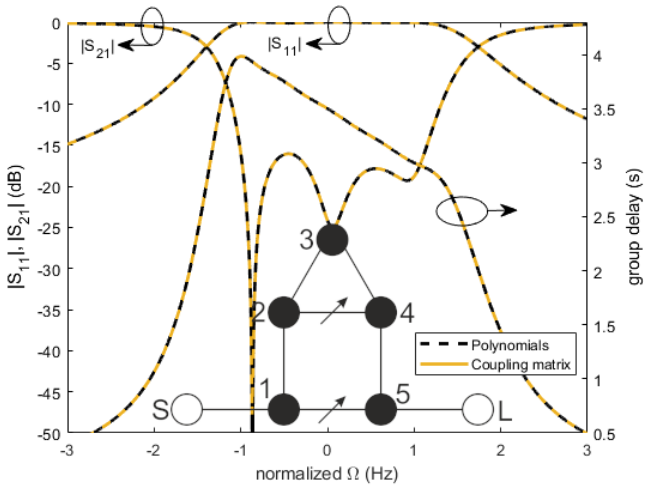

Fig. 3. Power-transmission ($|S_{21}|$), reflection ($|S_{11}|$), and group-delay responses of the fifth-order filter-based DDS example with negative group-delay slope calculated from polynomials (dashed lines) and the coupling matrix (solid lines)—its associated coupling-routing diagram is provided in the inset (black circles: resonators; white circles: source and load; lines: couplings; lines with arrows: FVCs).

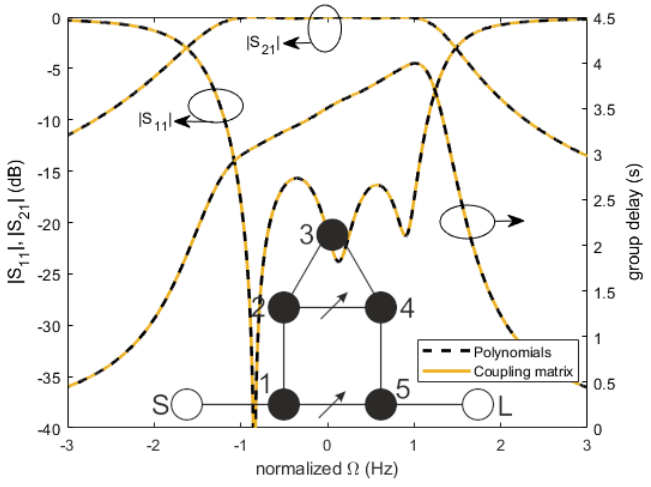

Fig. 4. Power-transmission ($|S_{21}|$), reflection ($|S_{11}|$), and group-delay responses of the fifth-order filter-based DDS example—waveguide DDS—with positive group-delay slope calculated from polynomials (dashed lines) and the coupling matrix (solid lines)—its associated coupling-routing diagram is provided in the inset (black circles: resonators; white circles: source and load; lines: couplings; lines with arrows: FVCs).

powerful and very-quickly converging zero-pole filter optimization technique [39]. Fig. 5 presents a comparison between the different target and simulated DDS characteristics, along with the waveguide-device model that is included in the inset.

TABLE III
ROOTS OF THE CHARACTERISTIC POLYNOMIALS OF THE FIFTH-ORDER WAVEGUIDE DDS

$E(s)$	$F(s)$	$P(s)$
$-0.6680 - 1.1984i$	$0.0075 - 0.8565i$	$1.1220 - 0.4673i$
$-0.8128 - 0.5013i$	$0.6711 - 0.5339i$	$-1.1220 - 0.4673i$
$-0.4726 + 1.1893i$	$0.1001 + 0.9347i$	$0.9291 + 0.8101i$
$-0.7911 + 0.1213i$	$0.5637 + 0.6200i$	$-0.9291 + 0.8101i$
$-0.6876 + 0.6846i$	$0.1602 + 0.1312i$	

The FVCs were implemented in the form of a metal post of incomplete height. Additionally, two tuning screws of 3-mm diameter were placed above the posts to allow for tuning in case that compensation for potential fabrication defects is needed.

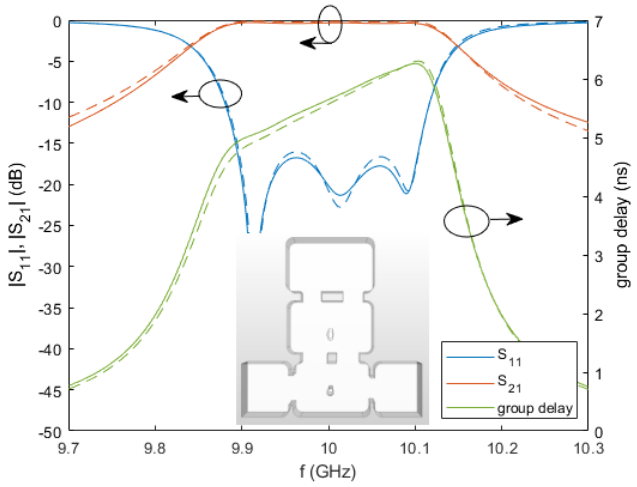

Fig. 5. Target and simulated power-transmission ($|S_{21}|$), reflection ($|S_{11}|$), and group-delay responses of the waveguide DDS (solid lines: simulation; dashed lines: target). The inset shows the 3D model in InventSim.

Fig. 6 shows the layout of the waveguide DDS with indication of dimensions. The height of the dispersive post between resonators 1 and 5 is $h_{15} = 7.34$ mm; the height of the dispersive post between resonators 2 and 4 is $h_{24} = 4.93$ mm; the corners of the waveguide cavities are rounded with a radius $r = 3$ mm. The value of the coupling between resonators 3 and 4 is negative, meaning that the phase of the signal passing through this resonator has to be reversed. Resonator 3 was thus designed to operate in the TE_{20} mode. The waveguide DDS prototype was manufactured using a CNC milling process from EN AW 2017 aluminum alloy with a fabrication tolerance of ± 50 μm and a surface-roughness parameter Ra equal to 1.6.

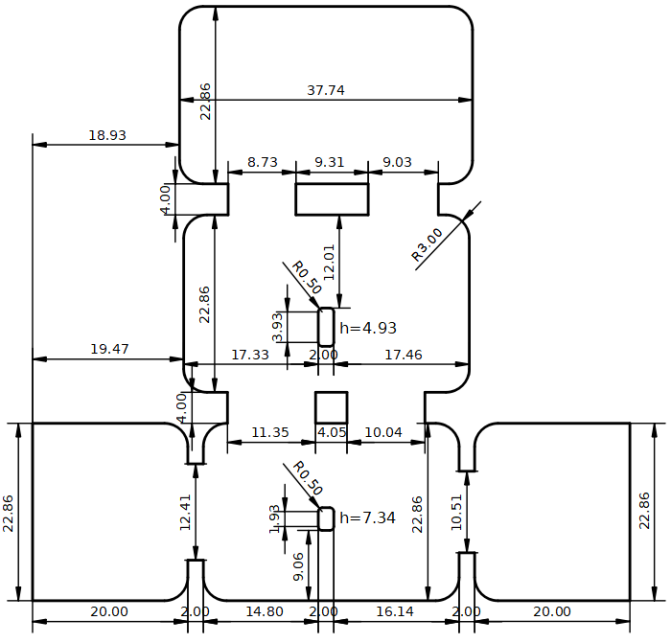

Fig. 6. Layout of the waveguide DDS with indication of dimensions (in mm).

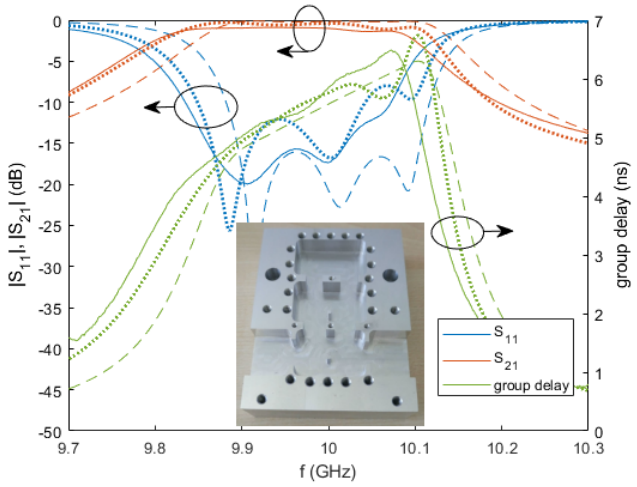

Fig. 7. Target, measured, and post-simulated power-transmission ($|S_{21}|$), reflection ($|S_{11}|$), and group-delay responses of the manufactured waveguide DDS prototype (solid lines: measurement; dashed line: target; dotted line: post-simulation with actual dimensions). The inset shows a photograph of the fabricated waveguide DDS circuit.

Fig. 7 provides a comparison between the target and measured power-transmission, reflection, and group-delay characteristics of the fabricated waveguide DDS, along with a photograph as an inset. As can be seen, the measured results of the physical device are shifted towards lower frequencies due to the imperfection of the manufacturing process. The measured bandwidth is equal to 235 MHz with a center frequency of 9.95 GHz and a minimum in-band power-insertion-loss level of 0.88 dB. The group-delay variation within the referred bandwidth is 2.24 ns, the slope coefficient is equal to 9.53 ns/GHz, and the resolution is $\varrho = 0.536$. To investigate the cause for the observed frequency shift, the manufactured waveguide DDS prototype was measured using a coordinate measuring machine. We found that the iris width between resonator 5 and the output access is significantly wider than the one assumed for the design—10.73 mm instead of 10.51 mm. Post-measurement simulations of the model with this wider iris width, which are also included in Fig. 7, corroborates that this is indeed the source of the referred frequency deviation as well as some deterioration of the in-band power-matching levels in the upper side of the passband. Nevertheless, the agreement obtained between measurements and simulations is considered to be reasonable enough to confirm the validity of this DDS design principle.

B. Third-Order Microstrip DDS

The second design example is a third-order coupled-resonator DDS device realized in microstrip technology. The center frequency of the circuit is $f_0 = 2$ GHz, the bandwidth is $BW = 140$ MHz, and the minimum in-band return-loss level for which the bandwidth is referred is $RL = 14.68$ dB—as obtained after polynomial optimization. The DDS structure has one frequency-dependent cross-coupling between resonators 1 and 3, which introduces a pair of complex TZs. The prescribed group-delay frequency-variation profile is linear and exhibits an in-band group-delay variation of $\Delta\tau = 0.67$ ns, a slope coefficient of 4.79 ns/GHz, and a resolution of $\varrho = 0.094$.

The polynomials and the initial coupling matrix were calculated by using the optimization-based procedure described in Section II. The poles and zeros of the characteristic function are summarized in Table IV. The different DDS characteristics calculated from both polynomials and the synthesized coupling matrix are compared in Fig. 8, where the corresponding coupling-routing diagram is also depicted as an inset. Again, the responses from both models are almost indistinguishable.

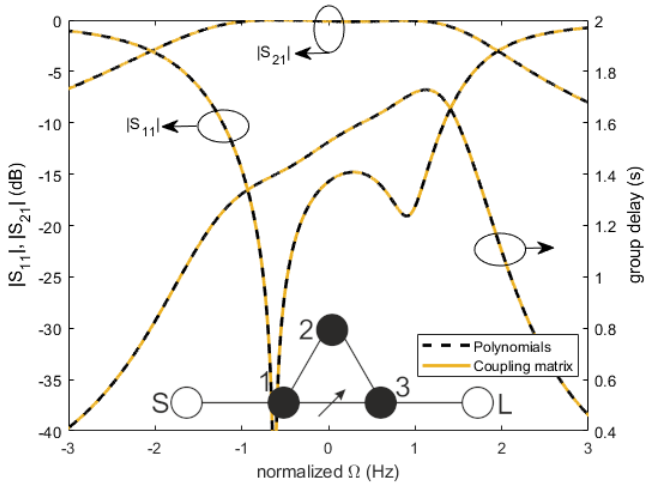

Fig. 8. Power-transmission ($|S_{21}|$), reflection ($|S_{11}|$), and group-delay responses of the third-order filter-based DDS example—microstrip DDS—with positive group-delay slope calculated from polynomials (dashed lines) and the coupling matrix (solid lines)—its associated coupling-routing diagram is provided in the inset (black circles: resonators; white circles: source and load; lines: couplings; lines with arrows: FVCs).

Since the circuit was intended to be implemented in microstrip technology, the initial coupling matrix was modified

TABLE IV
ROOTS OF THE CHARACTERISTIC POLYNOMIALS OF THE THIRD-ORDER MICROSTRIP DDS

$E(s)$	$F(s)$	$P(s)$
$-1.7444 - 1.2046i$	$1.3602 - 0.0087i$	$1.7634 + 0.6995i$
$-0.9360 + 1.3829i$	$0.1345 + 1.0236i$	$-1.7634 + 0.6995i$
$-1.4301 + 0.2818i$	$0.0000 - 0.5548i$	

to simplify the design and fabrication processes. The slope coefficient of the dispersive coupling—i.e., coefficient of ω at position $(4, 2)$ of the coupling matrix—is negative. This type of coupling can be realized in the form of a series short-ended stub [29]. However, it would be more convenient to use a shunt open-ended stub for it, but such stub can only introduce a positive slope. To overcome this issue, the second row and column of the coupling matrix were multiplied by -1. This conferred the dispersive coupling a positive slope, but gave all others couplings negative signs. To compensate for this effect, $90°$-electrical-length transmission-line sections were added to the resonators that are coupled through the dispersive stub.

Considering that the FVC was chosen to be implemented as an open-ended shunt stub, it was appropriate to exploit the technique reported in [29] to find a suitable coupling matrix for such structure. It provides more-accurate results than a general synthesis algorithm [37] by accounting for the loading effects of adjacent resonators due to the presence of the stub. Thus, this approach allows us to compensate for the effect of the stubs by adjusting the resonance frequencies of the resonators that are coupled by means of this stub. It leads to a very good starting point to proceed further with the design process. The modified coupling matrix has the form of (10), from which the initial design was simulated and numerically tuned in ADS Momentum software. The microstrip topology of this DDS design and its desired and simulated power-transmission, reflection, and group-delay responses are shown in Fig. 9.

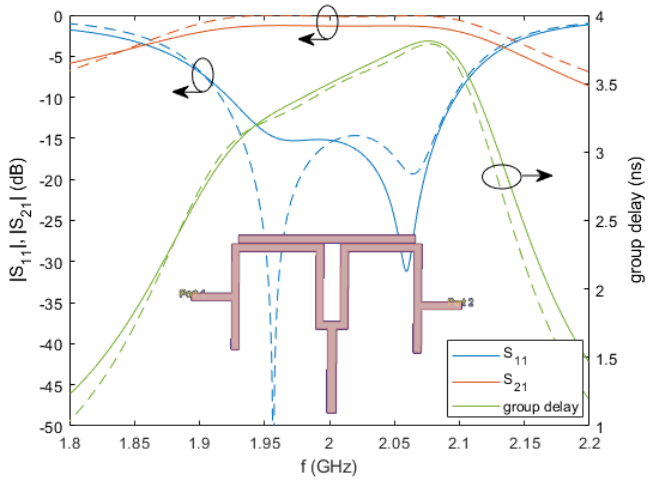

Fig. 9. Target and simulated power-transmission ($|S_{21}|$), reflection ($|S_{11}|$), and group-delay responses of the third-order microstrip DDS (solid lines: simulation; dashed lines: target). The inset shows the model in InventSim.

The microstrip DDS circuit was manufactured on a substrate with dielectric thickness $h = 0.762$ mm, relative dielectric permittivity $\epsilon_r = 3.48$, and dielectric loss tangent $\tan(\delta_D) = 0.0018$. The layout of the prototype with indication of dimensions is provided in Fig. 10.

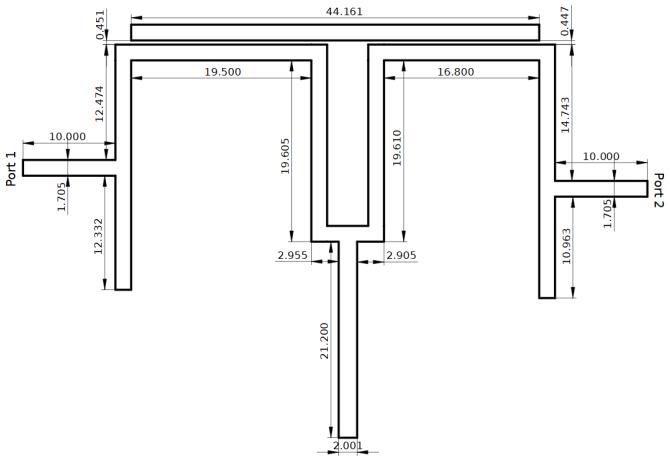

Fig. 10. Layout of the third-order microstrip DDS with indication of dimensions (in mm).

A comparison between the simulated and measured power-transmission, reflection, and group-delay characteristics of the developed third-order microstrip DDS is shown in Fig. 11. A photograph of the built prototype is also included as an inset. The main measured performance metrics of this microstrip DDS device are as follows: center frequency equal to 2 GHz, bandwidth of 129 MHz—referred to the measured minimun in-band return-loss level of 14.19 dB—, and minimum in-band power-insertion-loss level of 1.22 dB. The measured group-delay response exhibits a maximum variation within the referred bandwidth of $\Delta\tau = 0.61$ ns, a slope coefficient of 4.72 ns/GHz, and a resolution of $\varrho = 0.078$. It should be noticed that the measured power-reflection characteristic is shifted towards lower frequencies by 2 MHz and the measured passband is 5 MHz narrower than in the simulated results. Such minor deviations are attributed to manufacturing tolerances or variations of the real dielectric permittivity value with regard to the assumed one. However, the measured group-delay response exhibits a reasonably-close agreement with the simulated one, thus validating the proposed DDS design principle.

C. Fifth-Order Microstrip DDS

As the third and final design example, a fifth-order microstrip coupled-resonator DDS circuit with a stepped-type group-delay characteristic has been developed. The group-delay profile has three different in-band sub-intervals, within each of which the delay value is assumed to be constant. That is, the group-delay curve follows as staircase-like frequency-variation pattern with a distinct constant value assigned to each sub-interval or step. This allows the frequency components of the processed signals to be distinguished by the extent to which they are delayed by the DDS. The circuit was designed with a a center frequency $f_0 = 2$ GHz and a bandwidth $BW = 200$ MHz. The minimum in-band return-loss level is 10.43 dB, as the value derived from the polynomial optimization process.

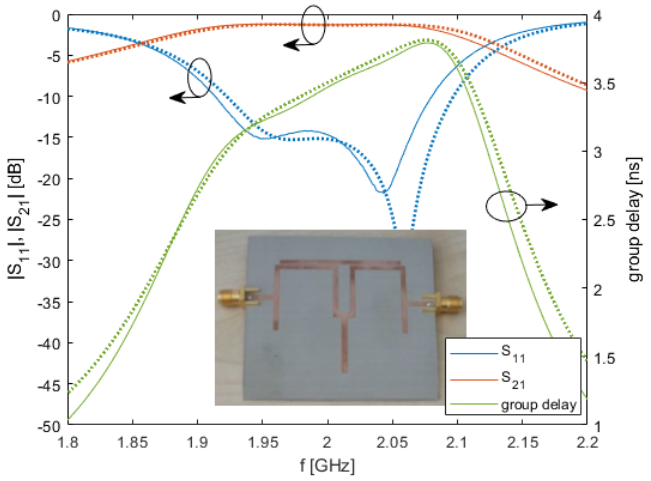

Fig. 11. Target and measured power-transmission ($|S_{21}|$), reflection ($|S_{11}|$), and group-delay responses of the manufactured third-order microstrip DDS prototype (solid lines: measurement; dotted lines: simulation;). The inset shows a photograph of the fabricated microstrip DDS circuit.

The group-delay characteristic is divided into three flat group-delay sub-intervals of 50-MHz bandwidth each. The delay value is not ideally flat within each sub-interval, but its variation over each of them is below 0.15 ns. The difference in the delay value between the steps is at least 0.3 ns. The parameters of the group-delay sub-intervals or steps are summarized in Table V. The maximum variation of the group delay within the overall bandwidth is equal to $\Delta\tau = 0.99$ ns and the resolution is $\varrho = 0.198$.

TABLE V
FREQUENCY RANGE AND MAXIMUM GROUP-DELAY VARIATION OF EACH STEP OF THE FIFTH-ORDER MICROSTRIP DDS (MEASURED VALUES IN BRACKETS)

Step number	Frequency range (GHz)	Group-delay variation (ns)
1	1.9–1.95 (1.861–1.93)	5–5.1 (5.02–5.17)
2	1.97–2.03 (1.95–2.01)	5.4–5.51 (5.45–5.6)
3	2.05–2.1 (2.03–2.06)	5.84–5.99 (5.93–6.08)

The synthesis process began with the calculation of the characteristic polynomials using the same procedure as in the previous design examples. The topology of the circuit includes two dispersive couplings—see the inset in Fig. 12—, which introduce two pairs of complex TZs. The roots of the polynomials are listed in Table VI. The power transmission, reflection, and group-delay characteristics resulting from the polynomial and coupling-matrix models are compared in Fig. 12, showing a nearly-perfect matching among them.

This fifth-order DDS design example was implemented in microstrip technology with the dispersive couplings realized through stubs. The procedure from [29], which was used in the previous example, was also applied here to determine the coupling matrix taking into account the loading effect. The final coupling matrix of the fifth-order DDS has the form shown in (11). The same microstrip substrate as in the previous example was used for circuit development. The layout of the fifth-order microstrip DDS is depicted in Fig. 13.

TABLE VI
ROOTS OF THE CHARACTERISTIC POLYNOMIALS OF THE FIFTH-ORDER MICROSTRIP DDS

$E(s)$	$F(s)$	$P(s)$
$-0.4374 + 1.1507i$	$0.7136 - 1.4206i$	$0.9466 + 0.6157i$
$-0.7591 - 1.6327i$	$0.2304 - 1.0095i$	$-0.9466 + 0.6157i$
$-0.5121 + 0.6088i$	$0.2400 + 0.8706i$	$1.2895 - 0.7745i$
$-0.5648 - 0.1342i$	$0.2189 + 0.7484i$	$-1.2895 - 0.7745i$
$-0.6787 - 0.9884i$	$0.0000 - 0.1846i$	

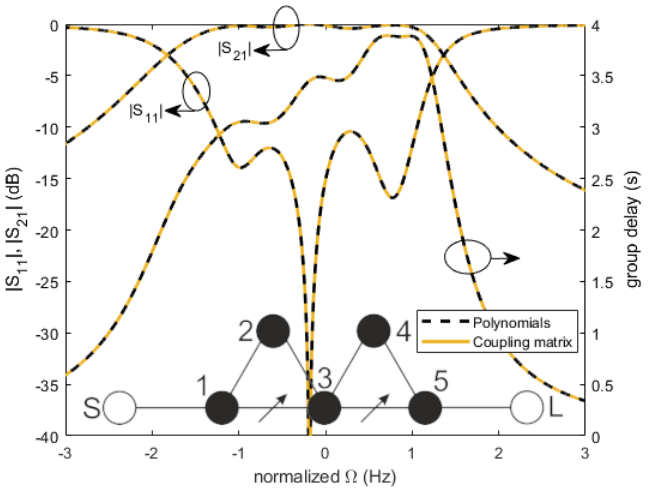

Fig. 12. Power-transmission ($|S_{21}|$), reflection ($|S_{11}|$), and group-delay responses of the fifth-order filter-based DDS example—microstrip DDS—with stepped-type group-delay pattern calculated from polynomials (dashed lines) and the coupling matrix (solid lines)—its associated coupling-routing diagram is provided in the inset (black circles: resonators; white circles: source and load; lines: couplings; lines with arrows: FVCs).

The DDS final dimensions were derived through numerical tuning with ADS Momentum simulator. The circuit topology of this fifth-order DDS design and its target and simulated power-transmission, reflection, and group-delay responses are represented in Fig. 14.

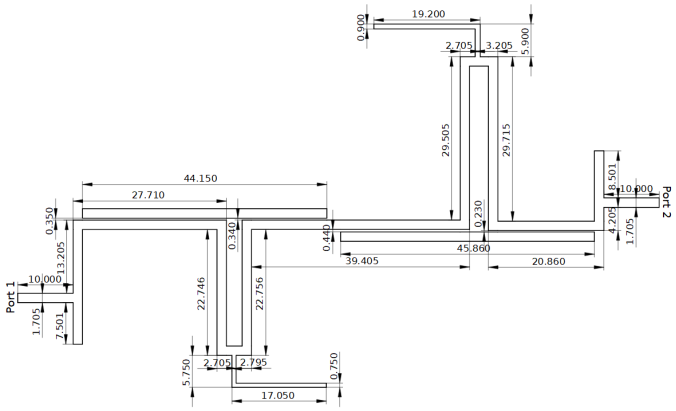

Fig. 13. Layout of the fifth-order microstrip DDS with indication of dimensions (in mm).

Fig. 15 shows the target and measured power-transmission, reflection, and group-delay curves of the built fifth-order microstrip DDS prototype, along with its photograph. The

TABLE VII
COMPARISON WITH MICROWAVE DDS DEVICES REPORTED IN THE TECHNICAL LITERATURE

Type of DDS	Technology	f_0 (GHz)	BW (MHz)	$\Delta\tau$ (ns)	Insertion loss (dB)	Asymmetry
C-section line [5]	Microstrip	5	2000	3.204	5	Yes
Reflection-type [17]	Microstrip	2.5	200	7	3.75	Yes
Coupled-resonator [23]	Waveguide	10	100	1.6	0.9	No
Coupled-resonator 1 (this work)	Waveguide	10	235	2.24	0.88	Yes
Coupled-resonator 2 (this work)	Microstrip	2	129	0.61	1.22	Yes
Coupled-resonator 3 (this work)	Microstrip	2	190	1.08	1.69	Yes

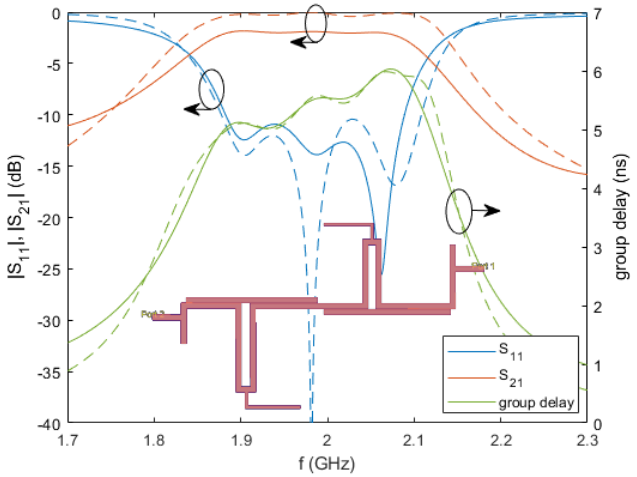

Fig. 14. Target and simulated power-transmission ($|S_{21}|$), reflection ($|S_{11}|$), and group-delay responses of the fifth-order microstrip DDS (solid lines: simulation; dashed lines: target). The inset shows the model in InventSim.

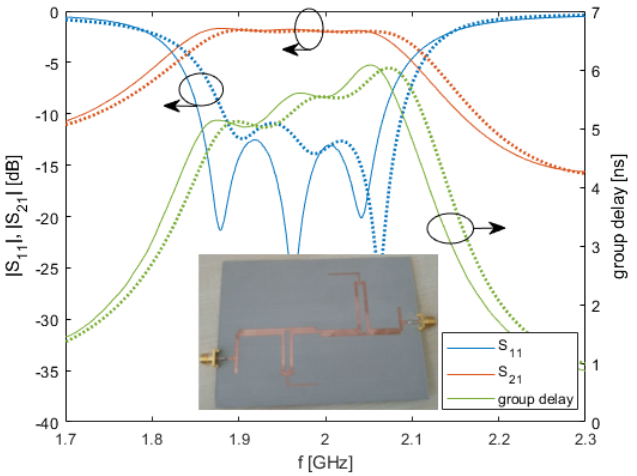

Fig. 15. Target and measured power-transmission ($|S_{21}|$), reflection ($|S_{11}|$), and group-delay responses of the manufactured fifth-order microstrip DDS prototype (solid lines: measurement; dotted lines: simulation;). The inset shows a photograph of the fabricated microstrip DDS circuit.

measured minimum in-band return-loss level is 12.52 dB. The measured bandwidth based on this return-loss-level value is 190 MHz with a center frequency of 1.96 GHz. The measured minimum in-band power-insertion-loss level is 1.69 dB. The measured values of the group-delay response are listed in Table V within brackets. In particular, the minimum group-delay-level difference between steps is 0.28 ns, the maximum group-delay variation within the operational bandwidth is $\Delta\tau = 1.08$ ns, and the resolution is equal to $\varrho = 0.211$. The measured response exhibits a 40-MHz shift towards lower frequencies, whose origin is due to the same reasons that were pointed out for the previous prototype.

D. Comparison With the State-of-the-Art

A comparison between the three DDS prototypes developed in this work and some related prior-art DDS devices reported in the technical literature is provided in Table VII. Whereas the C-section-based broad-band planar solution in [5] shows a low group-delay slope and high insertion loss as limitations, the narrower-band reflection-type DDS in [17] features larger group-delay swing but also exhibits high transmission loss. Moreover, it needs an external device to separate the input and output signals, which increases overall design complexity and size. On the other hand, the coupled-resonator-based DDS approach in [23] does not allows the patterning of asymmetrical-type group-delay profiles as one of the main design purposes of this work. Therefore, it is revealed by this comparative analysis that the engineered DDS circuits offer the best trade-off solution in terms of various of these performance metrics, such as group-delay shaping flexibility, insertion loss, avoidance of extra circuitry, and experimental validation in both microstrip and waveguide technologies. Furthermore, this is the first time that coupled-resonator networks with FVCs are applied to the design of microwave DDSs.

V. CONCLUSION

This paper has presented an optimization-based procedure for designing generalized DDSs with asymmetric-type group-delay response exploiting coupled-resonator networks with frequency-variant cross-couplings. We also discussed the synthesis of the characteristic polynomials allowing their initial modeling and the subsequent derivation of the corresponding coupling matrix. The proposed DDS design methodology has been validated through several examples, as well as with the fabrication and testing of three prototypes in waveguide and microstrip technologies featuring linear- and stepped-type group-delay frequency patterns.

ACKNOWLEDGMENT

The authors would like to thank Dr. L. Szydlowski for developing the topologies presented in Figs. 2(b) and 4 for

the initial design of the waveguide DDS.

REFERENCES

[1] M. Laso, T. Lopetegi, M. Erro, D. Benito, M. Garde, M. Muriel, M. Sorolla, and M. Guglielmi, "Real-time spectrum analysis in microstrip technology," *IEEE Trans. Microw. Theory Techn.*, vol. 51, no. 3, pp. 705–717, Mar. 2003.

[2] S. Gupta and C. Caloz, "Analog real-time Fourier transformer using a group delay engineered C-Section all-pass network," in *Proc. 2010 IEEE Int. Symp. Antennas Propag.*, Jul. 2010, pp. 1–4.

[3] T. Guo, Q. Zhang, Y. Chen, R. Wang, and C. Caloz, "Single-step tunable group delay phaser for spectrum sniffing," *IEEE Microw. Wireless Compon. Lett.*, vol. 25, no. 12, pp. 808–810, Dec. 2015.

[4] S. Abielmona, S. Gupta, and C. Caloz, "Experimental demonstration and characterization of a tunable CRLH delay line system for impulse/continuous wave," *IEEE Microw. Wireless Compon. Lett.*, vol. 17, no. 12, pp. 864–866, Dec. 2007.

[5] B. Nikfal, Q. Zhang, and C. Caloz, "Enhanced-SNR impulse radio transceiver based on phasers," *IEEE Microw. Wireless Compon. Lett.*, vol. 24, no. 11, pp. 778–780, Nov. 2014.

[6] J. D. Schwartz, J. Azana, and D. V. Plant, "A fully electronic system for the time magnification of ultra-wideband signals," *IEEE Trans. Microw. Theory Techn.*, vol. 55, no. 2, pp. 327–334, Feb. 2007.

[7] ——, "An electronic temporal imaging system for compression and reversal of arbitrary UWB waveforms," in *Proc. 2008 IEEE Radio Wireless Symp.*, Jan. 2008, pp. 487–490.

[8] B. Nikfal and C. Caloz, "Low-complexity and frequency-scalable analog real-time FDM receiver based on a dispersive delay structure," in *Proc. 2011 41st Eur. Microw. Conf.*, Oct. 2011, pp. 397–400.

[9] G. Zhang, Q. Zhang, F. Yang, Y. Chen, C. Caloz, and R. D. Murch, "Phaser-based feeding network for uniformly scanning antenna arrays," in *Proc. 2015 IEEE Int. Symp. Antennas Propag. and USNC-URSI Radio Science Meeting*, Jun.-Jul. 2015, pp. 236–237.

[10] L. Zou, S. Gupta, and C. Caloz, "Real-time dispersion code multiple access for high-speed wireless communications," *IEEE Trans. Wireless Commun.*, vol. 17, no. 1, pp. 266–281, Jan. 2018.

[11] C. Caloz, S. Gupta, Q. Zhang, and B. Nikfal, "Analog signal processing: A possible alternative or complement to dominantly digital radio schemes," *IEEE Microw. Mag.*, vol. 14, no. 6, pp. 87–103, Sep.-Oct. 2013.

[12] B. Nikfal, D. Badiere, M. Repeta, B. Deforge, S. Gupta, and C. Caloz, "Distortion-less real-time spectrum sniffing based on a stepped group-delay phaser," *IEEE Microw. Wireless Compon. Lett.*, vol. 22, no. 11, pp. 601–603, Nov. 2012.

[13] J. Schwartz, J. Azana, and D. Plant, "Experimental demonstration of real-time spectrum analysis using dispersive microstrip," *IEEE Microw. Wireless Compon. Lett.*, vol. 16, no. 4, pp. 215–217, Apr. 2006.

[14] M. Laso, T. Lopetegi, M. Erro, D. Benito, M. Garde, M. Muriel, A. Sorolla, and M. Guglielmi, "Chirped delay lines in microstrip technology," *IEEE Microw. Wireless Compon. Lett.*, vol. 11, no. 12, pp. 486–488, Nov. 2001.

[15] Q. Zhang, S. Gupta, and C. Caloz, "Synthesis of narrowband reflection-type phasers with arbitrary prescribed group delay," *IEEE Trans. Microw. Theory Techn.*, vol. 60, no. 8, pp. 2394–2402, Aug. 2012.

[16] T. Guo, Q. Zhang, Y. Chen, R. Wang, and C. Caloz, "Shunt-stub and stepped-impedance broadband reflective phasers," *IEEE Microw. Wireless Compon. Lett.*, vol. 26, no. 10, pp. 807–809, Oct. 2016.

[17] W. Liao, Q. Zhang, Y. Chen, S. Wong, and C. Caloz, "Compact reflection-type phaser using quarter-wavelength transmission line resonators," *IEEE Microw. Wireless Compon. Lett.*, vol. 25, no. 6, pp. 391–393, Jun. 2015.

[18] S. Gupta, A. Parsa, E. Perret, R. V. Snyder, R. J. Wenzel, and C. Caloz, "Group-delay engineered noncommensurate transmission line all-pass network for analog signal processing," *IEEE Trans. Microw. Theory Techn.*, vol. 58, no. 9, pp. 2392–2407, Sep. 2010.

[19] S. Gupta, D. L. Sounas, H. V. Nguyen, Q. Zhang, and C. Caloz, "CRLH–CRLH C-section dispersive delay structures with enhanced group-delay swing for higher analog signal processing resolution," *IEEE Trans. Microw. Theory Techn.*, vol. 60, no. 12, pp. 3939–3949, Dec. 2012.

[20] Q. Zhang, J. W. Bandler, and C. Caloz, "Design of dispersive delay structures (DDSs) formed by coupled C-sections using predistortion with space mapping," *IEEE Trans. Microw. Theory Techn.*, vol. 61, no. 12, pp. 4040–4051, Dec. 2013.

[21] A. Lujambio, I. Arnedo, M. Chudzik, I. Arregui, T. Lopetegi, and M. A. G. Laso, "Dispersive delay line with effective transmission-type operation in coupled-line technology," *IEEE Microw. Wireless Compon. Lett.*, vol. 21, no. 9, pp. 459–461, Sep. 2011.

[22] Q. Zhang and C. Caloz, "Alternative construction of the coupling matrix of filters with non-paraconjugate transmission zeros," *IEEE Microw. Wireless Compon. Lett.*, vol. 23, no. 10, pp. 509–511, Oct. 2013.

[23] Q. Zhang, D. L. Sounas, and C. Caloz, "Synthesis of cross-coupled reduced-order dispersive delay structures (DDSs) with arbitrary group delay and controlled magnitude," *IEEE Trans. Microw. Theory Techn.*, vol. 61, no. 3, pp. 1043–1052, Mar. 2013.

[24] S. Amari and J. Bornemann, "Using frequency-dependent coupling to generate finite attenuation poles in direct-coupled resonator bandpass filters," *IEEE Microw. Wireless Compon. Lett.*, vol. 9, no. 10, pp. 404–406, Oct. 1999.

[25] S. Amari, M. Bekheit, and F. Seyfert, "Notes on bandpass filters whose inter-resonator coupling coefficients are linear functions of frequency," in *Proc. 2008 IEEE MTT-S Int. Microw. Symp.*, Jun. 2008, pp. 1207–1210.

[26] M. Politi and A. Fossati, "Direct coupled waveguide filters with generalized Chebyshev response by resonating coupling structures," in *Proc. 2010 40th Eur. Microw. Conf.*, Sep. 2010, pp. 966–969.

[27] L. Szydlowski, A. Lamecki, and M. Mrozowski, "Coupled-resonator waveguide filter in quadruplet topology with frequency-dependent coupling—A design based on coupling matrix," *IEEE Microw. Wireless Compon. Lett.*, vol. 22, no. 11, pp. 553–555, Nov. 2012.

[28] L. Szydlowski, N. Leszczynska, A. Lamecki, and M. Mrozowski, "A substrate integrated waveguide (SIW) bandpass filter in a box configuration with frequency-dependent coupling," *IEEE Microw. Wireless Compon. Lett.*, vol. 22, no. 11, pp. 556–558, Nov. 2012.

[29] L. Szydlowski, N. Leszczynska, and M. Mrozowski, "Generalized Chebyshev bandpass filters with frequency-dependent couplings based on stubs," *IEEE Trans. Microw. Theory Techn.*, vol. 61, no. 10, pp. 3601–3612, Oct. 2013.

[30] ——, "A linear phase filter in quadruplet topology with frequency-dependent couplings," *IEEE Microw. Wireless Compon. Lett.*, vol. 24, no. 1, pp. 32–34, Jan. 2014.

[31] L. Szydlowski and M. Mrozowski, "A self-equalized waveguide filter with frequency-dependent (resonant) couplings," *IEEE Microw. Wireless Compon. Lett.*, vol. 24, no. 11, pp. 769–771, Nov. 2014.

[32] S. Tamiazzo and G. Macchiarella, "Synthesis of cross-coupled filters with frequency-dependent couplings," *IEEE Trans. Microw. Theory Techn.*, vol. 65, no. 3, pp. 775–782, Mar. 2016.

[33] P. Zhao and K. Wu, "Cascading fundamental building blocks with frequency-dependent couplings in microwave filters," *IEEE Trans. Microw. Theory Techn.*, vol. 67, no. 4, pp. 1432–1440, Apr. 2019.

[34] G. Macchiarella, G. G. Gentili, N. Delmonte, L. Silvestri, and M. Bozzi, "Design of inline waveguide filters with frequency-variant couplings producing transmission zeros," *IEEE Trans. Microw. Theory Techn.*, vol. 69, no. 8, pp. 3746–3658, Aug. 2021.

[35] M. Y. Sandhu, Z. Ahmed, S. Hyder, and S. Afridi, "Inline integrated ceramic waveguide bandpass filter with $N + 1$ finite transmission zeros," *IETE J. Research*, pp. 1–7, 2020.

[36] Y. Zhang, F. Seyfert, S. Amari, M. Olivi, and K.-L. Wu, "General synthesis method for dispersively coupled resonator filters with cascaded topologies," *IEEE Trans. Microw. Theory Techn.*, vol. 69, no. 2, pp. 1378–1393, Feb. 2021.

[37] L. Szydlowski, A. Lamecki, and M. Mrozowski, "Coupled-resonator filters with frequency-dependent couplings: Coupling matrix synthesis," *IEEE Microw. Wireless Compon. Lett.*, vol. 22, no. 6, pp. 312–314, Jun. 2012.

[38] J.-S. Hong and M. J. Lancaster, *Microstrip Filters for RF/Microwave Applications*. John Wiley & Sons, Ltd, 2001, ch. 8, pp. 235–272.

[39] L. Balewski, G. Fotyga, M. Mrozowski, M. Mul, P. Sypek, D. Szypulski, and A. Lamecki, "Step on it!: Bringing fullwave finite-element microwave filter design up to speed," *IEEE Microw. Mag.*, vol. 21, no. 3, pp. 34–49, Mar. 2020.